Efficient and Highly Stable 3D Printed NiFe and NiCo Bifunctional Electrodes for Practical HER and OER

Jeoffrey Tourneur, Loïc Joanny, Loïc Perrin, Stéphane Paul, Bruno Fabre

Efficient and Highly Stable 3D Printed NiFe and NiCo Bifunctional Electrodes for Practical HER and OER

Jeoffrey Tourneur[1,2], Loïc Joanny[3], Loïc Perrin[2,*], Stéphane Paul[2], and Bruno Fabre[1,*]

[1] Jeoffrey Tourneur and Bruno Fabre – CNRS, ISCR (Institut des Sciences Chimiques de Rennes) – UMR6226, Univ Rennes, Rennes F-35000, France.

[2] Jeoffrey Tourneur, Loïc Perrin and Stéphane Paul – SAS H2X Ecosystems - High Park II - 10, rue Louis Blériot, 35170 Bruz, France

[3] Loïc Joanny – Univ. Rennes, CNRS, ScanMAT-CMEBA-UMS2001, F-35000, France

KEYWORDS: *Water splitting, Hydrogen Evolution reaction (HER), Oxygen Evolution Reaction (OER), Alkaline Electrolysis, 3D Printing, Electrocatalysis*

ABSTRACT: Considered like a fully renewable and clean energy carrier with the highest energy density, dihydrogen (H_2) constitutes the best alternative to fossil fuels for insuring the sustainability of energy. This technologically and industrially relevant energy vector can be produced by water electrolysis that is now widely recognized as an eco-friendly, scalable and carbon-free route. In that context, alkaline water electrolysis is an affordable technology because it allows the use of transition metals as electrocatalysts for both hydrogen (HER) and oxygen (OER) evolution reactions. Here, combining catalytically active transition metal alloys (NiFe and NiCo) with a 3D printing technique, namely selective laser melting (SLM), enables access to ca. 25 cm^2 microstructured cylindrical electrodes efficiently promoting alkaline HER and OER. NiCo is found to be the most efficient electrode for HER, with an overpotential of 210 mV at 10 mA cm^{-2}. It is also the most stable electrode when studied in operation during prolonged electrolysis with a potential change of only 40 mV after 140 h electrolysis at 50 mA cm^{-2} (1.25 A). Regarding OER, NiFe shows the highest catalytic activity with an overpotential of 300 mV at 10 mA cm^{-2} and the greatest stability in operation with an electrolysis-induced potential change of only 30 mV. Further surface characterization techniques (scanning electron microscopy SEM, energy dispersive X-ray spectroscopy EDS, contact angle measurements, and analysis of electrogenerated gas bubbles) are used to monitor the electrolysis-induced chemical changes and to get valuable information on the bubble dynamics. Interestingly, electrolysis is found to be beneficial for enhancing the hydrophilicity/aerophobicity of the electrodes and thus facilitating the detachment of the H_2 or O_2 bubbles.

1 Introduction

In the context of an increase in worldwide energy consumption of about 60 % from 2010 to 2040[1], it becomes crucial to develop large-scale economically viable technological processes to produce and store energy. Facing traditional fossil fuels responsible for climate change and global warming, dihydrogen H_2 constitutes a clean energy carrier and sustainable alternative for meeting future energy demands[2]. Nowadays, H_2 can be used either as an energy vector owing to its high mass energy density (123 MJ kg^{-1}), or as a chemical reagent for Haber-Bosch process[3]. As an energy vector, it can be consumed into a fuel cell to produce electricity for mobility[4], or to store the excess energy produced by intermittent and renewable energy sources[5]. Around 95% of the global H_2 production still relies on methane steam reforming which leads to the emission of greenhouse gases such as carbon dioxide and carbon monoxide[6,7]. The generation of H_2 by water electrolysis is now widely recognized as a clean and carbon-free route[8–10]. However, this process is still costly and cannot become affordable as long as it uses scarce and noble metals such as Pt, Pd, Ir, Ru as electrode materials[11]. These metals are principally employed for PEM (Proton Exchange Membrane) electrolysis in acidic medium[1,12] . This type of electrolyzer yields the highest current densities for H_2 production but is prone to corrosion owing to the harsh oxidizing conditions in the anodic compartment. Research continues to explore alkaline water (AWE) and anion exchange membrane (AEM) electrolyzers because these technologies allow the use of transition metals as electrocatalysts for both hydrogen (HER) and oxygen (OER) evolution reactions[13,14]. Transition metals are generally widespread and quite cheap, in addition to offer a high electrocatalytic efficiency competing with that of Pt group metals[15,16] . A benchmarking study by Jaramillo and co-workers has enabled to evaluate and standardize the HER and OER electrocatalytic activity of numerous electrodeposited Ni-based binary alloys (incorporating Co, Cr, Mo, Fe, La or W) [17,18]. Other groups have also shown that ternary alloys, such as NiCoFe[19,20], NiCoMo[21], NiCrMo[22], NiFeMo[23] and NiFeCr[24], could be excellent

candidates for electrocatalyzing these two half-reactions of interest. In these alloys, each metal plays a key role with a positive impact on electrocatalysis. For instance, Mo shows a high affinity to adsorb protons while Ni can dissociate water[25]. The precise role of Fe is still in discussion, it could either act as an active site for the reaction, or activate it[26,27]. Co alloyed with Ni yields a bifunctional material able to electrocatalyze both alkaline HER and OER. Concerning Cr, its presence enables the catalytic alloy to be effectively protected against corrosion[28,29]. These catalytic materials are usually deposited on conducting (metal foam or carbon) substrates by either electrochemical or hydrothermal methods from the corresponding metal salts[30,31]. Although these simple and fast methods allow the catalyst structure to be controlled at the nanometer scale, their industrial scale-up is however not so easy.

In that context, 3D printing has appeared as an emerging technique to produce a new kind of metal components with complex geometries[32,33]. 3D printing offers numerous advantages such as the opportunities of preparing metallic alloys with customized composition, novel and complex electrode shapes and porous systems with high resolution and high control on the surface microstructure. Among the different 3D printing methods, the SLM (Selective Laser Melting) technique is particularly suitable to print different types of metals. The principle of SLM is based on the local melting of metal by a high-power laser beam scanning over a metal powder bed in a controlled manner (Figure 1). Thus, metal pieces with complex geometries can be fabricated layer-by-layer with a resolution between two layers of 20 μm. Some groups, such as Pumera et al[34–36] and Esposito et al[37,38], have already used this additive manufacturing technology to print electrodes or electrolyzers with original geometries.

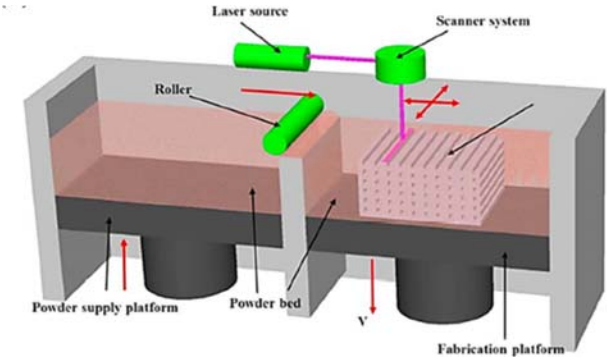

Figure 1. Schematic illustration of the metal additive manufacturing with a metal powder bed employing SLM (Selective Laser Melting) technology. Reproduced with permission from reference 32. Copyright 2018 Elsevier.

SLM has a current resolution of about 100 μm and can routinely printed 10 cm-sized metal pieces. This technology is already used for aeronautics industry and its development towards the energy sector remains still to be explored. Indeed, although the 3D printing methods hold great promises to fabricate practical catalytic electrodes[39], their use to elaborate metallic alloys specifically designed for electrochemical purposes has not been yet explored to the best of our knowledge[39,40].

In this work, ca. 25 cm^2 cylindrical NiFe and NiCo electrodes have been printed by SLM from the mixture of the corresponding metal powders. Their electrocatalytic performance for both HER and OER in alkaline medium has been examined and compared with that of reference Ni cylinder. Interestingly, it is also demonstrated that the introduction of cylindrical micropatterns on the electrode surface was an efficient strategy to facilitate the gas bubbles release. Moreover, complementary surface characterization techniques have been used to investigate the chemical changes of the electrodes caused by their prolonged cathodic or anodic polarization.

2 Experimental Section

2.1 Chemicals

Spherical powders for 3D printing of Ni (purity 99.99 %, 15-35 μm granulometry) was purchased from Hoganas. Spherical powders for 3D printing of Fe and Co (purity 99.99 %, 15-53 μm granulometry) were purchased from Neyco. KOH (>85 %, analysis grade) and absolute ethanol (RSE grade) were purchased from Sigma-Aldrich and Carlo Erbatron, respectively. Ultra-pure water (Veolia Water-STI) with a resistivity of 18.2 MΩ cm was used to prepare the aqueous solutions.

2.2 3D printing

All electrodes were designed using the software Auto Desk Fusion 360. Magics software was used for implementation on the platform using block and contour supports. A Turbula T2F station was used to mix the atomic powders in a powder bed of NiFe and NiCo. Electrodes were produced by SLS France company using the SLM technique in a TechGine TS120 under nitrogen atmosphere. Each layer of melt metal was 20 μm-thick. The so fabricated electrodes were then removed from the support, scraped and sand, then cleaned under pressurized air. Photographs of these electrodes are shown in Figure S1 (Supporting Information).

2.3 Electrochemistry

The electrochemical measurements were performed at room temperature on a HTDS PARSTAT PMC-200 multichannel electrochemical workstation equipped with an AC frequency response analyzer (FRA). The 3D printed electrode was directly used as the working electrode (geometric surface area: 25 cm^2). A graphite rod or a double stabilized anode (DSA, model AO2002, titanium foil covered by mixed ruthenium and iridium oxides, ECS Tarn) was used as the counter electrode for OER or HER, respectively. The reference electrode was either Hg/HgO from Origalys for chronopotentiometry or KCl-saturated Ag/AgCl for cyclic voltammetry. For comparison, a pure Ni electrode (25 cm^2 geometric surface area) was considered. Before use, the working electrode was sonicated for 10 min in ultra-pure water and absolute ethanol to remove the oxide layer and was dried at 70°C for 3 h. An electrical contact was established with an ergot on the electrode and masked with an insulating epoxy resin (Loctite EA9460, Ellswoth Additives). The electrode was then placed into an oven at 90°C overnight to cure the resin.

A home-made H-type electrochemical macrocell with a constant headspace volume was used to carry out long-term

electrolytic tests at high current intensities with ca. 25 cm^2 electrodes (Figure S2). The macrocell consisted of two compartments with a total electrolyte capacity of 1.4 L, in order to neglect the volume consumed during the water electrolysis. The headspace volume was 1.25 L per half-cell, so that volume changes caused by the produced gas (H_2 and O_2) could be neglected. This large headspace volume was chosen to avoid overpressure during GC analysis. The cell was sealed by a flat and circular ground joint, closed by a stainless steel flange. The junction was made by a male-female ground joint sealed with Teflon tape. Septa and epoxy resin (Loctite, EA3423, Ellswoth Additives) were used to seal the openings for gas measurement and introduction of the working electrode.

All cyclic voltammograms (CVs) were recorded at 5 mV s^{-1} and the Ohmic drop was corrected using the cell resistance determined at high frequencies (typically 100 kHz). The corresponding Tafel slopes were determined from the linear overpotential vs. log (current density) (η vs. log j) plots. The current densities were normalized by the geometric surface area of the 3D printed electrodes determined with Auto Desk Fusion 360 software and all the measured potentials were converted versus the reversible hydrogen electrode (RHE) according to the equations given below:

In an alkaline medium (1.0 M KOH, pH = 14 ± 0.1) using a Hg/HgO reference electrode (filled with 0.1 M KOH solution):

$$E_{RHE} = E_{Hg/HgO} + 0.059\ pH + E^0_{Hg/HgO}$$

$$\text{with } E^0_{Hg/HgO} = +0.14\ V \quad (1)$$

In an alkaline medium (1.0 M KOH, pH = 14 ± 0.1) using an Ag/AgCl reference electrode (filled with saturated KCl solution):

$$E_{RHE} = E_{Ag/AgCl} + 0.059\ pH + E^0_{Ag/AgCl}$$

$$\text{with } E^0_{Ag/AgCl} = +0.20\ V \quad (2)$$

where $E_{Hg/HgO}$ and $E_{Ag/AgCl}$ are the applied potential values versus the selected reference electrode. Potentials are given with 5 mV precision and the reference electrodes were controlled every six months[41].

Electrochemical impedance spectroscopy (EIS) measurements were performed at an applied overpotential of 0.1 V for HER and 0.3 V for OER over a frequency range from 100 kHz to 100 mHz (50 frequencies, logarithmic distribution) at 10 mV amplitude. The long-term stability of the catalytic electrodes was examined using chronopotentiometry at an applied ±50 mA cm^{-2} current density. EIS data were analyzed using the Zview software.

2.4 Characterizations

Scanning electron microscopy (SEM) images and EDS (Energy Dispersive X-Ray Spectroscopy) elemental mapping were performed using a IT-300 JEOL microscope and an X-Max 50 mm^2 EDS detector (Oxford Instruments).

Profilometry measurements were performed using a Bruker Dektak X profilometer with a Stylus B type tip (12.5 µm curvature radius) and tilt angle correction.

ICP-AES (Inductive Coupled Plasma Atomic Emission Spectroscopy) measurements were performed using a 725 ES Varian station with an argon plasma.

Static water contact angles were measured with an automated Krüss Easy Drop goniometer. At least three small droplets of 2.0 μL of ultra-pure water were dispensed, and the contact angles were determined using a Tangent 2 fitting model.

Gas chromatography (GC) measurements for the detection and quantification of the gases produced by electrolysis were performed with a micro-GC Agilent 990 equipped with a TCD detector. The column was heated at 145°C, the injector at 90°C, with Alphagaz 2 Smartop argon (Air Liquide) as the carrier gas at 29 psi. Sampling time was 50 ms and the results are obtained in vol. %. For the determination of the Faradaic efficiency (FE), the apparatus was calibrated with a gas mixture containing N_2 (3%, v/v), CH_4 (5%, v/v), CO (10%, v/v), H_2 (10%, v/v), CO_2 (20%, v/v) and He (52%, v/v) (from GazDetect, UN1954) and air from the laboratory. A H-type cell perfectly closed was used and degassed under Ar for 10 min prior to analysis. A current density of ±10 mA cm^{-2} was applied during 1.5 h and one measurement was realized every 10 min. The current density was selected considering the theoretical gas production to not exceed 10% of the headspace volume of the cell. The FE was determined using the gas perfect law and the pressure value measured by a Vernier sensor. It was expressed versus a reference material (Pt for HER and DSA for OER) studied under the same conditions. We have checked that a 1 cm^2 Pt sheet or DSA grid immersed in ca. 100 mL electrochemical cell and polarized at ± 10 mA yielded FEs of 100% for HER and OER, respectively.

2.5 Bubble dynamics

Pictures of the electrode covered with hydrogen bubbles were acquired at 35 frames per second with a ThorLabs CS165MU/M camera equipped with a MVL35M23 objective. Screenshots from the videos were processed using the freeware Image J to estimate the average surface coverage and the size of the bubbles.

3 Results and Discussion

3.1 Characterization of 3D printed binary alloys

The morphological characteristics and composition of 25 cm^2 3D printed materials were evaluated by profilometry, SEM and EDS. First, profilometry measurements revealed rough surfaces with an average roughness of 5.0 ± 1.3 μm irrespective of the composition of the binary alloy. It is worth emphasizing that high roughness is a main characteristic of the SLM technique[42]. Dimensions of the cylindrical patterns engraved on the electrode surface ranged from 200 to 300 μm for their height, 700 to 800 μm and 400 to 500 µm for their vertical and horizontal elongations, respectively (Figure S3). The chemical composition and its homogeneity were determined by SEM-EDS at the micrometer scale (Figure 2). NiCo showed a homogeneous distribution of Ni and Co elements (Figure S4). The Co content was estimated at 10% from EDS. In contrast, Ni and Fe were not homogeneously distributed in the NiFe alloy and two phases were clearly evidenced: *i*) one phase showing Fe microparticles of 20-30 μm diameter (red large areas in Figure 2) and

ii) a second one characterized by μm-sized Fe particles in a Ni matrix (red dots in the green area). The average Fe content was around 6%.

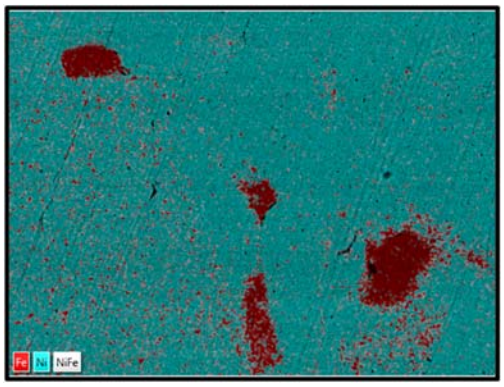

Figure 2. EDS elemental mapping of NiFe showing the inhomogeneous distribution of Ni (blue) and Fe (red).

3.2 Hydrogen Evolution Reaction

3.2.1 Electrocatalytic activity and stability

The electrocatalytic activity of the 25 cm^2 3D printed electrodes was evaluated in alkaline medium (1.0 M KOH, pH 14) both for HER and OER. Based on the electrochemical surface area of these electrodes, it is worth emphasizing that current intensities as high as 1 A could be delivered.

Before the HER process, a reversible redox wave corresponding to the formation and oxidation of nickel hydrides[43] was observed within the potential range 0.0-0.3 V vs RHE for the three electrodes (Figure S5). This wave was followed by the HER one starting below ca. -0.1 V vs RHE (Figure 3a). NiCo exhibited the highest HER activity, as supported by the lowest *iR*-corrected overpotential of 210 mV measured at 10 mA cm^{-2} (250 mA) (Table 1). This value was 20 and 60 mV lower than those determined for Ni and NiFe, respectively. Comparable Tafel slopes between 89 (Ni) and 103 mV per decade (NiFe) were determined, in relatively close agreement with those reported for Ni-based HER cathodes studied in alkaline medium [23,25,35,44].

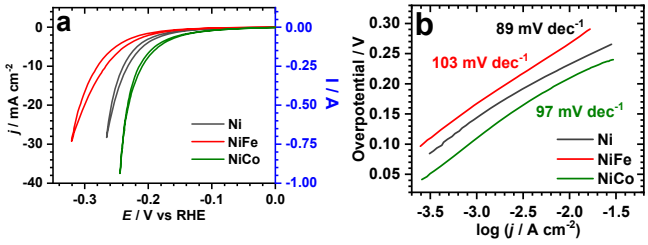

Figure 3. a) Ohmic drop-corrected cyclic voltammograms of Ni, NiFe and NiCo at 5 mV s^{-1} in KOH 1M. b) Corresponding Tafel plots.

Table 1. Key Performance Indicators (KPIs) Measured for Ni, NiFe and NiCo for Hydrogen Evolution Reaction.

Cathode	Ni	NiFe	NiCo
η_{-10} / mV [a]	230	270	210
Tafel slope / mV dec^{-1}	89	103	97
Faradaic efficiency / %	88	92	90
Electrolysis-induced potential change / mV [b]	100	100	40
R_s / mΩ cm^{-2} [c]	7.2	7.2	9.2
R_{ct} / mΩ cm^{-2} [c]	280	454	215

[a] HER overpotential at -10 mA cm^{-2}. [b] After 140 h electrolysis at -50 mA cm^{-2}. [c] At -0.1 V vs RHE.

In order to gain further insights on the electron transfer kinetics, EIS measurements were performed at an applied overpotential of 0.1 V and in the frequency range 10^5-10^{-1} Hz. The data are presented as plots of the imaginary part (Z'') vs the real part (Z') of the complex impedance ($Z = Z' + iZ''$) as a function of frequency f (Nyquist diagram). All Nyquist plots are characterized by a semicircle and can be reasonably fitted by assuming the equivalent electrical circuit comprising a resistance (the cell resistance R_s) in series with the charge transfer resistance (R_{ct}) and a constant phase element (CPE) in parallel (Figure 4a). For this circuit model, the diameter of the semicircle on the Z' axis corresponds to R_{ct}. Moreover, CPE is responsible for the deformation of the semi-circle in the diagram due to a frequency dispersion of the capacitance and accounts for surface inhomogeneities such as roughness or structuration[45–47]. Consistent with CV data, the R_{ct} of the NiCo electrode (215 mΩ cm^{-2}) was found to be smaller than that calculated for Ni (280 mΩ cm^{-2}) and NiFe (454 mΩ cm^{-2}) demonstrating faster HER charge transfer kinetics (Table 1).

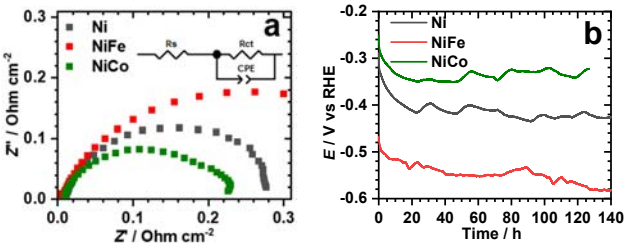

Figure 4. a) Nyquist plots at -0.1 V vs RHE for Ni, NiFe and NiCo from 100 kHz to 100 mHz and equivalent electrical circuit used for fitting (inset). b) Chronopotentiometric curves at -50 mA cm^{-2} for Ni, NiFe and NiCo in KOH 1M.

The long-term stability of 3D printed cathodes was examined at a constant current density of -50 mA cm^{-2} over six days. The corresponding chronopotentiometric curves showed that NiCo was stabilized at a less negative potential (namely -0.33 V vs RHE) with respect to the two other electrodes (Figure 4b). It was also the most robust electrode as the potential change was only 40 mV after 140 h electrolysis, while a potential change of 100 mV was monitored for Ni and NiFe.

FE for HER was about 90% vs reference Pt for the three electrodes (Figure S6 and Table 1). This value lower than

100% could be reasonably explained by the large-scale electrodes and the large headspace volume of the cell leading to unavoidable loss of produced gas. Moreover, it is noticeworthy that the temperature of the electrolytic solution increased by 7°C after electrolysis which could also account for a non- quantitative FE for HER.

3.2.2 Bubble dynamics

Among the factors influencing the yield of an electrolyzer, the efficiency of the release of H_2 and O_2 bubbles produced at the cathode and anode, respectively, represents a critical issue for high-performance electrocatalysis. This problem is often minimized in laboratory-scale electrochemical cells by using small electrode surfaces of less than 1 cm^2. This constitutes however a major issue in industry, as bubble films formed at large scale (a few dozen to a few hundred tens cm^2) electrodes can be more than 1 cm thick, leading to high Ohmic resistances and mass transfer barriers of the electrode reactions, and consequently resulting in a strong enhancement in the electrical power consumption of the electrolyzer[48,49]. Consequently, the control of both the nucleation and the flow of gas bubbles is a crucial issue to optimize electrolysis process and reduce costs. In that context, the N. S. Lewis' group produced some valuable data about this topic[48,50]. The electrode microstructuring, in the form of e.g. conic arrays[51], canals[52], or microwires[50], and the surface functionalization[53,54] have been demonstrated to be promising approaches to control the aerophobicity of the surface and thus the bubble release[55].

In this study, photographs have been captured from videos recorded during the electrolysis of 3D printed cathodes. Two current densities were selected, namely -1 and -30 mA cm^{-2}, in order to observe the nucleation phase of bubbles and their detachment from the electrode surface when a high density of bubbles was electrogenerated. Effects of the long-term electrolysis on the efficiency of the bubbles release were also investigated. Globally, the characteristics of H_2 bubbles electrogenerated at -1 mA cm^{-2} on freshly prepared electrodes were not dependent on the nature of the electrode (Figures 5 and S7). The electrode surface was covered by about 5% of H_2 bubbles and the average radius of one bubble was 55 ± 15 μm (determined from the image processing by the ImageJ freeware, Figure S8). After a long-term electrolysis at -50 mA cm^{-2} for 140 h, the photographs showed a vertically directed bubble cloud with few bubbles remaining on the electrode surface. This apparent facilitated release of H_2 bubbles caused by electrolysis was thought to be ascribed to the enhanced hydrophilicity/aerophobicity of the electrodes. Indeed, the contact angles measured with KOH 1M for the three electrodes were dramatically decreased from ca. 110° to 30° ± 5° after electrolysis.

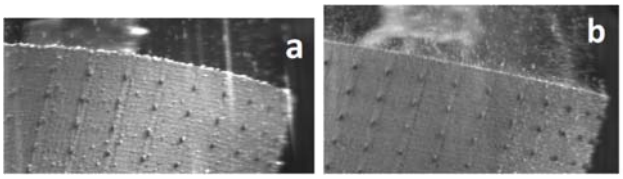

Figure 5. Photographs of the best performing NiCo electrode for HER at -1 mA cm^{-2} in KOH 1M before (a) and after (b) long-term electrolysis at -50 mA cm^{-2} for 140 h.

A plausible reason for the enhanced aerophobicity of the electrodes could be the formation of nickel hydrides due to the hydrogen diffusion into Ni, which is commonly observed for Ni electrodes studied for HER in alkaline medium[43]. At -30 mA cm^{-2}, approximately 80% of the micropatterns acted as coalescence sites of H_2 bubbles (Figure S9, movie 1). The mean bubble departure radius was estimated to be 120 ± 30 μm. After electrolysis, only 10-15% of the patterns were still covered by bubbles with unchanged departure radius (movie 2).

3.2.3 Post-electrolysis characterizations

Different surface characterization techniques have been used to monitor the potential morphology and composition changes of the electrodes caused by 140 h electrolysis at -50 mA cm^{-2}. First, post-electrolysis profilometry analysis confirmed that cylindrical micropatterns geometry and dimensions remained unchanged. Some lower atomic number phases were now visible on NiCo and NiFe to a lesser extent which were evidenced by the darker areas on the backscattered electron SEM images (Figure 6). The EDS analysis showed that the metallic composition of the three electrodes was not significantly altered after electrolysis (Table S1). It was however noticed an increase in the O content and the presence of potassium varying from 2 at. % (Ni and NiFe) to 15% (NiCo). These results are consistent with the adsorption of potassium carbonates on the electrode surface and are not surprising in sofar as such species were systematically detected for Ni-based HER and OER catalysts polarized in alkaline KOH medium[17]. Although all the detected elements were homogeneously distributed on the electrode surface in the case of Ni and NiFe, two distinct phases could be distinguished for NiCo (Figures S10-S12). The Ni and Co contents of the majority phase were relatively close to those before electrolysis while the second one which was poor in metals and rich in K and O was probably composed of potassium carbonates. It is obvious that these two chemically different phases were responsible for the bright and dark areas, respectively, in the backscattered electron SEM images (Figure 6).

Finally, the ICP-AES analysis of the electrolytic solution showed the absence of released metals after electrolysis.

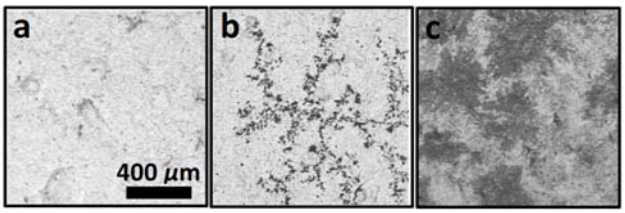

Figure 6. Large-scale backscattered electron SEM images of Ni (a), NiFe (b) and NiCo (c) after electrolysis at -50 mA cm^{-2} for 140 h.

3.3 Oxygen Evolution Reaction

3.3.1 Electrocatalytic activity and stability

The same protocol as that used for HER was followed for measuring the electrocatalytic activity of the three 3D printed electrodes for OER. Before OER, a scan rate-dependent reversible redox wave (Ni^{3+}/Ni^{2+}) was first observed for all anodes between 1.2 and 1.5 V vs RHE, corresponding to

the oxidation of Ni hydroxide to NiOOH[43] which is the catalytically active species for OER (Figure S5)[56,57]. An additional anodic peak was also visible at ca. 1.2 V for NiCo which could be also ascribed to the conversion of Co hydroxide to its oxyhydroxide form[58]. This transition metal hydroxide/oxyhydroxide redox process was followed by the OER signal displaying a much larger current density (Figure 7a). NiFe showed an overpotential for OER of 300 mV at 10 mA cm^{-2} which was lower than those measured for Ni and NiCo (~350 mV) (Table 2). The higher efficiency of NiFe for OER was confirmed by its Tafel slope of 33 mV per decade (Figure 7b) which was smaller than those of NiCo (40 mV per decade) and Ni (63 mV per decade). It is worth noting that such values were in perfect line with those determined for other Ni-based OER electrocatalysts deposited on nickel foam or stainless steel[35,44].

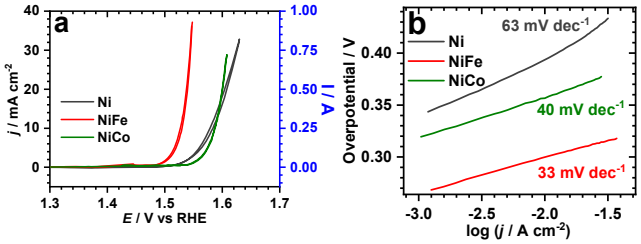

Figure 7. a) Ohmic drop-corrected cyclic voltammograms of Ni, NiFe, and NiCo at 5 mV s^{-1} in KOH 1M. b) Corresponding Tafel plots.

Table 2. KPIs Measured for Ni, NiFe and NiCo for Oxygen Evolution Reaction.

Anode	Ni	NiFe	NiCo
η_{+10} / mV [a]	350	300	360
Tafel slope / mV dec^{-1}	63	33	40
Faradaic efficiency / %	100	100	100
Electrolysis-induced potential change / mV [b]	90	30	100
R_s / mΩ cm^{-2} [c]	6.0	7.2	7.2
R_{ct} / mΩ cm^{-2} [c]	20.0	6.0	87.2

[a] OER overpotential at +10 mA cm^{-2}. [b] After 140 h electrolysis at +50 mA cm^{-2}. [c] At 1.5 V vs RHE.

Faster OER charge transfer kinetics of NiFe was also assessed by the R_{ct} value of 6.0 mΩ cm^{-2} extracted from Nyquist plots which was much smaller than those determined for Ni (20.0 mΩ cm^{-2}) and NiCo (87.2 mΩ cm^{-2}) (Figure 8a). Additionally, NiFe showed a relatively good catalytic stability under operation. Long-term electrolysis at +50 mA cm^{-2} for 140 h revealed that NiFe was the most robust anode as the potential change was only 30 mV after 140 h electrolysis, while potential changes of 90 and 100 mV were monitored for Ni and NiCo, respectively (Figure 8b).

FE for OER was 100% vs reference DSA for the three electrodes (Figure S13). Nevertheless, it can be noticed that the FE of DSA was only 83% vs the theoretical FE calculated from the consumed electrical charge. This discrepancy can be reasonably explained by the large headspace volume and the increase in the electrolyte temperature during electrolysis, as mentioned before for HER.

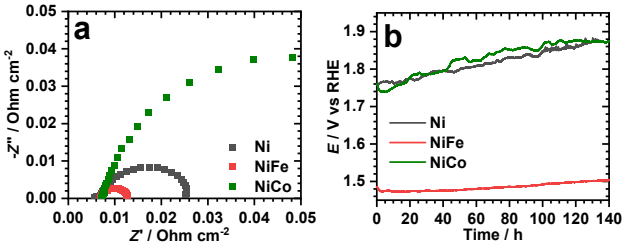

Figure 8. a) Nyquist plots at 1.5 V vs RHE for Ni, NiFe and NiCo from 100 kHz to 100 mHz. b) Chronopotentiometric curves at +50 mA cm^{-2} for Ni, NiFe and NiCo in KOH 1M.

3.3.2 Bubble dynamics

Globally, the surface coverage of O_2 bubbles electrogenerated at +1 mA cm^{-2} was lower than that of H_2 bubbles (Figures 9 and S14) which is quite logical given that two moles of H_2 are produced for one mole of O_2 in the overall water splitting. Furthermore, the mean bubble nucleation and departure radii were not significantly different from those estimated for HER (Figure S15). After a long-term electrolysis at +50 mA cm^{-2} for 140 h, the bubbles were more easily released from the electrode surface, as a result of the increased hydrophilicity/aerophobicity of the electrodes. Indeed, similar to HER, the contact angles measured with KOH 1M for the three electrodes were decreased from ca. 110° to 30° ± 5° after electrolysis. Such a trend can be explained by the formation of metal hydroxides/oxyhydroxides during the electrolysis[59]. At +30 mA cm^{-2}, very few bubbles were observed on the electrode surface either before or after electrolysis (Figure S16, movies 3 and 4). Moreover, a careful examination of bubbles photographs showed that the flow of released O_2 bubbles was higher for NiFe and NiCo than for Ni at both +1 and +30 mA cm^{-2}.

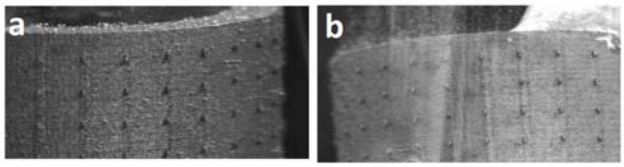

Figure 9. Photographs of the best performing NiFe electrode for OER at +1 mA cm^{-2} in KOH 1M before (a) and after (b) long-term electrolysis at +50 mA cm^{-2} for 140 h.

3.3.3 Post-electrolysis characterizations

As for HER, the profilometry analysis of the three electrodes after 140 h electrolysis at +50 mA cm^{-2} showed no significant changes in the engraved micropatterns geometry and dimensions. A slight decrease in the content of Ni was observed for Ni and NiFe whereas the metallic composition of NiCo remained stable (Table S2). The analysis by ICP-AES of the electrolytic solution after electrolysis revealed that metallic Ni was released from the Ni and NiFe electrodes at the level of traces, i.e 60-200 ppm. Consistent with these findings, chemically different phases were clearly evidenced by backscattered electron SEM for Ni (Figure 10). The darker areas corresponded to phases richer in O and poorer in K in the EDS map (Figure S17) and therefore could be reasonably ascribed to Ni oxides. In contrast, all the

detected elements were globally homogeneously distributed on the NiFe and NiCo surfaces (Figures S18 and S19).

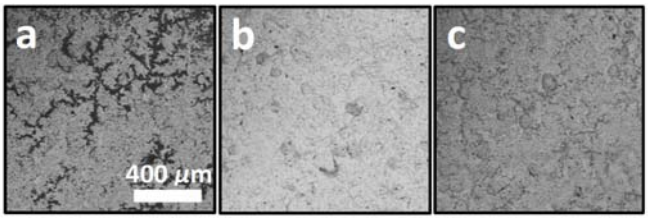

Figure 10. Large-scale backscattered electron SEM images of Ni (a), NiFe (b) and NiCo (c) after electrolysis at +50 mA cm^{-2} for 140 h.

4 Conclusion

To sum-up, ca. 25 cm^2 cylindrical Ni, NiFe and NiCo electrodes were fabricated by 3D printing technique and their electrocatalytic performance for alkaline HER and OER was evaluated. Nearly cylindrical micropillars engraved on the electrode surface acted as preferential sites for the nucleation of the electrogenerated gas bubbles. Regarding HER, NiCo was found to be the most efficient and the most stable electrode when studied in operation during electrolysis at -50 mA cm^{-2} (-1.25 A) over 140 h. Compared with Ni and NiFe, this result was somewhat surprising if one considers that the chemical composition of this material was the most strongly modified after electrolysis with a higher proportion of adsorbed potassium carbonates in particular. For the other half-reaction, NiFe showed a superior OER activity and stability in operation. Furthermore, the chemical composition of the bimetallic alloys was not significantly changed after 140 h electrolysis at +50 mA cm^{-2}. Interestingly, electrolysis was found to be beneficial for enhancing the hydrophilicity/aerophobicity of the electrodes and thus facilitating the detachment of the H_2 or O_2 bubbles.

This work constitutes a first promising step towards practical and industrially relevant functional electrodes able to deliver current intensities higher than 1 A for electrolytic water splitting. By taking the advantage of the versatility of the SLM technique, other Ni-based bi- and trimetallic alloys with different geometry and structuring will be envisaged in order to enhance the catalytic performance and stability in operation. In that context, the resolution of the engraved micropatterns is still low and needs to be increased in the future to reach the micrometer scale. This is a necessary step to finely control the flow and the detachment of the electrogenerated gas bubbles, and consequently the efficiency of the electrolyzer. Work in this stimulating direction is currently in progress.

ASSOCIATED CONTENT

Supporting Information. Supplementary profilometry curves, SEM-EDS mapping, photographs and analysis of the electrogenerated gas bubbles, GC chromatograms and additional cyclic voltammograms. This material is available free of charge via the Internet at http://pubs.acs.org.

AUTHOR INFORMATION

Corresponding Author

* Loïc Perrin: loic.perrin@h2x-ecosystems.com
* Bruno Fabre: bruno.fabre@univ-rennes.fr

Author Contributions

B. F., L.P. and J. T. conceived the project and designed the experiments, J.T. performed experiments and analyzed the data. B. F. and J.T. wrote the manuscript. All authors contributed to the results discussion. All authors participated in editing the paper and have given approval to the final version of the manuscript. The SEM measurements have been performed on CMEBA platforms (ScanMAT, UAR 2025 University of Rennes-CNRS; CPER-FEDER 2015-2020) by L.J. The authors declare no competing financial interest.

Funding Sources

ANRT (Agence Nationale de la Recherche Technologique) and H2X Ecosystems are acknowledged to fund this work through the CIFRE program.

Notes

Due to the industrial work, the SLM process laser parameters and Auto Desk Fusion instructions for the patterning of the electrodes are protected and under confidentiality for submitting further patent.

ACKNOWLEDGMENT

Muriel Escadeillas (CRMPO, Univ. Rennes) is fully acknowledged for ICP-AES measurements performed at CRMPO platform. Axel Dubois and Hugo Schaal (CEO, SLS France) are fully acknowledged for their contribution to the fabrication of the 3D printed electrodes.

ABBREVIATIONS

AEM, Alkaline Exchange Membrane; AWE, Alkaline Water Electrolysis; CPE, Constant Phase Element; DSA, Double Stabilized Anode; EDS, Energy Dispersive X-Ray Spectroscopy; EIS, Electrochemical Impedance Spectroscopy; FE, Faradaic Efficiency; HER, Hydrogen Evolution Reaction; ICP-AES, Inductive Coupled Plasma Atomic Emission Spectroscopy; KPI, Key Performance Indicator; OER, Oxygen Evolution Reaction; PEM, Proton exchange Membrane; SEM, Scanning Electron Microscopy; SLM, Selective Laser Melting.

REFERENCES

(1) Lewis, N. S.; Nocera, D. G. Powering the Planet: Chemical Challenges in Solar Energy Utilization. *Proc. Natl. Acad. Sci.* **2006**, *103* (43), 15729–15735. https://doi.org/10.1073/pnas.0603395103.
(2) International Energy Agency. The Future of Hydrogen, 2019.
(3) Ghahraloud, H.; Farsi, M.; Rahimpour, M. R. Hydrogen Production through Thermal Decomposition of Hydrogen Sulfide: Modification of the Sulfur Recovery Unit To Produce Ultrapure Hydrogen. *Ind. Eng. Chem. Res.* **2018**, *57* (42), 14114–14123. https://doi.org/10.1021/acs.iecr.8b01407.
(4) Acar, C.; Dincer, I. The Potential Role of Hydrogen as a Sustainable Transportation Fuel to Combat Global Warming. *Int. J. Hydrog. Energy* **2020**, *45* (5), 3396–3406. https://doi.org/10.1016/j.ijhydene.2018.10.149.
(5) Tourneur, J.; Fabre, B.; Loget, G.; Vacher, A.; Mériadec, C.; Ababou-Girard, S.; Gouttefangeas, F.; Joanny, L.; Cadot, E.; Haouas, M.; Leclerc-Laronze, N.; Falaise, C.; Guillon, E. Molecular and Material Engineering of Photocathodes Derivatized with Polyoxometalate-Supported {Mo3S4} HER Catalysts. *J. Am.*

Chem. Soc. **2019**, *141* (30), 11954–11962. https://doi.org/10.1021/jacs.9b03950.
(6) United States Department of Energy. A National Vision of America's Trasition to a Hydrogen Economy - to 2030 and Beyond., 2003. www.ogel.org/article.asp?key=743.
(7) European Commission. A Hydrogen Strategy for a Climate Neutral Europe [COM(2020) 301 Final], 2020.
(8) Terlouw, T.; Bauer, C.; McKenna, R.; Mazzotti, M. Large-Scale Hydrogen Production *via* Water Electrolysis: A Techno-Economic and Environmental Assessment. *Energy Environ. Sci.* **2022**, *15* (9), 3583–3602. https://doi.org/10.1039/D2EE01023B.
(9) Kang, Y.; Cretu, O.; Kikkawa, J.; Kimoto, K.; Nara, H.; Nugraha, A. S.; Kawamoto, H.; Eguchi, M.; Liao, T.; Sun, Z.; Asahi, T.; Yamauchi, Y. Mesoporous Multimetallic Nanospheres with Exposed Highly Entropic Alloy Sites. *Nat. Commun.* **2023**, *14* (1), 4182. https://doi.org/10.1038/s41467-023-39157-2.
(10) Jiang, B.; Guo, Y.; Sun, F.; Wang, S.; Kang, Y.; Xu, X.; Zhao, J.; You, J.; Eguchi, M.; Yamauchi, Y.; Li, H. Nanoarchitectonics of Metallene Materials for Electrocatalysis. *ACS Nano* **2023**, *17* (14), 13017–13043. https://doi.org/10.1021/acsnano.3c01380.
(11) Cao, J.; Li, H.; Pu, J.; Zeng, S.; Liu, L.; Zhang, L.; Luo, F.; Ma, L.; Zhou, K.; Wei, Q. Hierarchical NiMo Alloy Microtubes on Nickel Foam as an Efficient Electrocatalyst for Hydrogen Evolution Reaction. *Int. J. Hydrog. Energy* **2019**, *44* (45), 24712–24718. https://doi.org/10.1016/j.ijhydene.2019.07.229.
(12) Shiva Kumar, S.; Himabindu, V. Hydrogen Production by PEM Water Electrolysis – A Review. *Mater. Sci. Energy Technol.* **2019**, *2* (3), 442–454. https://doi.org/10.1016/j.mset.2019.03.002.
(13) Ehlers, J. C.; Feidenhans'l, A. A.; Therkildsen, K. T.; Larrazábal, G. O. Affordable Green Hydrogen from Alkaline Water Electrolysis: Key Research Needs from an Industrial Perspective. *ACS Energy Lett.* **2023**, *8* (3), 1502–1509. https://doi.org/10.1021/acsenergylett.2c02897.
(14) Yu, Z.; Duan, Y.; Feng, X.; Yu, X.; Gao, M.; Yu, S. Clean and Affordable Hydrogen Fuel from Alkaline Water Splitting: Past, Recent Progress, and Future Prospects. *Adv. Mater.* **2021**, *33* (31), 2007100. https://doi.org/10.1002/adma.202007100.
(15) Trasatti, S. Work Function, Electronegativity, and Electrochemical Behaviour of Metals. *J. Electroanal. Chem. Interfacial Electrochem.* **1972**, *39* (1), 163–184. https://doi.org/10.1016/S0022-0728(72)80485-6.
(16) Roger, I.; Shipman, M. A.; Symes, M. D. Earth-Abundant Catalysts for Electrochemical and Photoelectrochemical Water Splitting. *Nat. Rev. Chem.* **2017**, *1* (1). https://doi.org/10.1038/s41570-016-0003.
(17) McCrory, C. C. L.; Jung, S.; Ferrer, I. M.; Chatman, S. M.; Peters, J. C.; Jaramillo, T. F. Benchmarking Hydrogen Evolving Reaction and Oxygen Evolving Reaction Electrocatalysts for Solar Water Splitting Devices. *J. Am. Chem. Soc.* **2015**, *137* (13), 4347–4357. https://doi.org/10.1021/ja510442p.
(18) McCrory, C. C. L.; Jung, S.; Peters, J. C.; Jaramillo, T. F. Benchmarking Heterogeneous Electrocatalysts for the Oxygen Evolution Reaction. *J. Am. Chem. Soc.* **2013**, *135* (45), 16977–16987. https://doi.org/10.1021/ja407115p.
(19) Barati Darband, Gh.; Aliofkhazraei, M.; Rouhaghdam, A. S. Facile Electrodeposition of Ternary Ni-Fe-Co Alloy Nanostructure as a Binder Free, Cost-Effective and Durable Electrocatalyst for High-Performance Overall Water Splitting. *J. Colloid Interface Sci.* **2019**, *547*, 407–420. https://doi.org/10.1016/j.jcis.2019.03.098.
(20) Bachvarov, V.; Lefterova, E.; Rashkov, R. Electrodeposited Ni-FeCo and NiFeCoP Alloy Cathodes for Hydrogen Evolution Reaction in Alkaline Medium. *Int. J. Hydrog. Energy* **2016**, *41* (30), 12762–12771. https://doi.org/10.1016/j.ijhydene.2016.05.164.
(21) Jeghan, S. M. N.; Kim, N.; Lee, G. Mo-Incorporated Three-Dimensional Hierarchical Ternary Nickel-Cobalt-Molybdenum Layer Double Hydroxide for High-Efficiency Water Splitting. *Int. J. Hydrog. Energy* **2021**, *46* (43), 22463–22477. https://doi.org/10.1016/j.ijhydene.2021.04.071.
(22) Nady, H.; El-Rabiei, M. M.; Samy, M.; Deyab, M. A.; Abd El-Hafez, G. M. Novel Ni–Cr-Based Alloys as Hydrogen Fuel Sources through Alkaline Water Electrolytes. *Int. J. Hydrog. Energy* **2021**, *46* (70), 34749–34766. https://doi.org/10.1016/j.ijhydene.2021.08.056.
(23) Hsieh, C.-T.; Huang, C.-L.; Chen, Y.-A.; Lu, S.-Y. NiFeMo Alloy Inverse-Opals on Ni Foam as Outstanding Bifunctional Catalysts for Electrolytic Water Splitting of Ultra-Low Cell Voltages at High Current Densities. *Appl. Catal. B Environ.* **2020**, *267*, 118376. https://doi.org/10.1016/j.apcatb.2019.118376.
(24) Yang, Y.; Dang, L.; Shearer, M. J.; Sheng, H.; Li, W.; Chen, J.; Xiao, P.; Zhang, Y.; Hamers, R. J.; Jin, S. Highly Active Trimetallic NiFeCr Layered Double Hydroxide Electrocatalysts for Oxygen Evolution Reaction. *Adv. Energy Mater.* **2018**, *8* (15), 1703189. https://doi.org/10.1002/aenm.201703189.
(25) Nairan, A.; Zou, P.; Liang, C.; Liu, J.; Wu, D.; Liu, P.; Yang, C. NiMo Solid Solution Nanowire Array Electrodes for Highly Efficient Hydrogen Evolution Reaction. *Adv. Funct. Mater.* **2019**, *29* (44), 1903747. https://doi.org/10.1002/adfm.201903747.
(26) Bao, F.; Kemppainen, E.; Dorbandt, I.; Xi, F.; Bors, R.; Maticiuc, N.; Wenisch, R.; Bagacki, R.; Schary, C.; Michalczik, U.; Bogdanoff, P.; Lauermann, I.; van de Krol, R.; Schlatmann, R.; Calnan, S. Host, Suppressor, and Promoter—The Roles of Ni and Fe on Oxygen Evolution Reaction Activity and Stability of NiFe Alloy Thin Films in Alkaline Media. *ACS Catal.* **2021**, *11* (16), 10537–10552. https://doi.org/10.1021/acscatal.1c01190.
(27) Feng, C.; Faheem, M. B.; Fu, J.; Xiao, Y.; Li, C.; Li, Y. Fe-Based Electrocatalysts for Oxygen Evolution Reaction: Progress and Perspectives. *ACS Catal.* **2020**, *10* (ngu), 4019–4047. https://doi.org/10.1021/acscatal.9b05445.
(28) Babu, S. P.; Falch, A. Recent Developments on Cr-Based Electrocatalysts for the Oxygen Evolution Reaction in Alkaline Media. *ChemCatChem* **2022**, *14* (15). https://doi.org/10.1002/cctc.202200364.
(29) Peng, L.; Min, J.; Bendavid, A.; Chu, D.; Lu, X.; Amal, R.; Han, Z. Stabilizing the Unstable: Chromium Coating on NiMo Electrode for Enhanced Stability in Intermittent Water Electrolysis. *ACS Appl. Mater. Interfaces* **2022**, *14* (36), 40822–40833. https://doi.org/10.1021/acsami.2c09004.
(30) Sobha Jayakrishnan, D. Electrodeposition: The Versatile Technique for Nanomaterials. In *Corrosion Protection and Control Using Nanomaterials*; Elsevier, 2012; pp 86–125. https://doi.org/10.1533/9780857095800.1.86.
(31) Feng, S.-H.; Li, G.-H. Hydrothermal and Solvothermal Syntheses. In *Modern Inorganic Synthetic Chemistry*; Elsevier, 2017; pp 73–104. https://doi.org/10.1016/B978-0-444-63591-4.00004-5.
(32) Ngo, T. D.; Kashani, A.; Imbalzano, G.; Nguyen, K. T. Q.; Hui, D. Additive Manufacturing (3D Printing): A Review of Materials, Methods, Applications and Challenges. *Compos. Part B Eng.* **2018**, *143*, 172–196. https://doi.org/10.1016/j.compositesb.2018.02.012.
(33) DebRoy, T.; Mukherjee, T.; Milewski, J. O.; Elmer, J. W.; Ribic, B.; Blecher, J. J.; Zhang, W. Scientific, Technological and Economic Issues in Metal Printing and Their Solutions. *Nat. Mater.* **2019**, *18* (10), 1026–1032. https://doi.org/10.1038/s41563-019-0408-2.
(34) Ambrosi, A.; Moo, J. G. S.; Pumera, M. Helical 3D-Printed Metal Electrodes as Custom-Shaped 3D Platform for Electrochemical Devices. *Adv. Funct. Mater.* **2016**, *26* (5), 698–703. https://doi.org/10.1002/adfm.201503902.
(35) Ambrosi, A.; Pumera, M. Multimaterial 3D-Printed Water Electrolyzer with Earth-Abundant Electrodeposited Catalysts. *ACS Sustain. Chem. Eng.* **2018**, *6* (12), 16968–16975. https://doi.org/10.1021/acssuschemeng.8b04327.
(36) Browne, M. P.; Redondo, E.; Pumera, M. 3D Printing for Electrochemical Energy Applications. *Chem. Rev.* **2020**, *120* (5), 2783–2810. https://doi.org/10.1021/acs.chemrev.9b00783.
(37) Esposito, D. V. Membraneless Electrolyzers for Low-Cost Hydrogen Production in a Renewable Energy Future. *Joule* **2017**, *1* (4), 651–658. https://doi.org/10.1016/j.joule.2017.07.003.

(38) Bui, J. C.; Davis, J. T.; Esposito, D. V. 3D-Printed Electrodes for Membraneless Water Electrolysis. *Sustain. Energy Fuels* **2020**, *4* (4), 213–225. https://doi.org/10.1039/C9SE00710E.
(39) Lee, C.-Y.; Taylor, A. C.; Nattestad, A.; Beirne, S.; Wallace, G. G. 3D Printing for Electrocatalytic Applications. *Joule* **2019**, *3* (8), 1835–1849. https://doi.org/10.1016/j.joule.2019.06.010.
(40) Liu, R.; Zhou, Z.; Xiao, R.; Yu, A. CFD-DEM Modelling of Mixing of Granular Materials in Multiple Jets Fluidized Beds. *Powder Technol.* **2020**, *361*, 315–325. https://doi.org/10.1016/j.powtec.2019.08.002.
(41) Kawashima, K.; Márquez, R. A.; Son, Y. J.; Guo, C.; Vaidyula, R. R.; Smith, L. A.; Chukwuneke, C. E.; Mullins, C. B. Accurate Potentials of Hg/HgO Electrodes: Practical Parameters for Reporting Alkaline Water Electrolysis Overpotentials. *ACS Catal.* **2023**, *13* (3), 1893–1898. https://doi.org/10.1021/acscatal.2c05655.
(42) Koutiri, I.; Pessard, E.; Peyre, P.; Amlou, O.; De Terris, T. Influence of SLM Process Parameters on the Surface Finish, Porosity Rate and Fatigue Behavior of as-Built Inconel 625 Parts. *J. Mater. Process. Technol.* **2018**, *255*, 536–546. https://doi.org/10.1016/j.jmatprotec.2017.12.043.
(43) Hall, D. S.; Bock, C.; MacDougall, B. R. The Electrochemistry of Metallic Nickel: Oxides, Hydroxides, Hydrides and Alkaline Hydrogen Evolution. *J. Electrochem. Soc.* **2013**, *160* (3), F235–F243. https://doi.org/10.1149/2.026303jes.
(44) Zhang, W.; Li, D.; Zhang, L.; She, X.; Yang, D. NiFe-Based Nanostructures on Nickel Foam as Highly Efficiently Electrocatalysts for Oxygen and Hydrogen Evolution Reactions. *J. Energy Chem.* **2019**, *39*, 39–53. https://doi.org/10.1016/j.jechem.2019.01.017.
(45) Pajkossy, T. Impedance Spectroscopy at Interfaces of Metals and Aqueous Solutions — Surface Roughness, CPE and Related Issues. *Solid State Ion.* **2005**, *176* (25–28), 1997–2003. https://doi.org/10.1016/j.ssi.2004.06.023.
(46) Jorcin, J.-B.; Orazem, M. E.; Pébère, N.; Tribollet, B. CPE Analysis by Local Electrochemical Impedance Spectroscopy. *Electrochimica Acta* **2006**, *51* (8–9), 1473–1479. https://doi.org/10.1016/j.electacta.2005.02.128.
(47) Hirschorn, B.; Orazem, M. E.; Tribollet, B.; Vivier, V.; Frateur, I.; Musiani, M. Determination of Effective Capacitance and Film Thickness from Constant-Phase-Element Parameters. *Electrochimica Acta* **2010**, *55* (21), 6218–6227. https://doi.org/10.1016/j.electacta.2009.10.065.
(48) Kempler, P. A.; Coridan, R. H.; Lewis, N. S. Effects of Bubbles on the Electrochemical Behavior of Hydrogen-Evolving Si Microwire Arrays Oriented against Gravity. *Energy Environ. Sci.* **2020**, *13* (6), 1808–1817. https://doi.org/10.1039/D0EE00356E.
(49) Zhao, X.; Ren, H.; Luo, L. Gas Bubbles in Electrochemical Gas Evolution Reactions. *Langmuir* **2019**, *35* (16), 5392–5408. https://doi.org/10.1021/acs.langmuir.9b00119.
(50) Kempler, P. A.; Ifkovits, Z. P.; Yu, W.; Carim, A. I.; Lewis, N. S. Optical and Electrochemical Effects of H_2 and O_2 Bubbles at Upward-Facing Si Photoelectrodes. *Energy Environ. Sci.* **2021**, *14* (1), 414–423. https://doi.org/10.1039/D0EE02796K.
(51) Ma, H.; Cao, M.; Zhang, C.; Bei, Z.; Li, K.; Yu, C.; Jiang, L. Directional and Continuous Transport of Gas Bubbles on Superaerophilic Geometry-Gradient Surfaces in Aqueous Environments. *Adv. Funct. Mater.* **2018**, *28* (7), 1705091. https://doi.org/10.1002/adfm.201705091.
(52) Bintein, P.-B.; Lhuissier, H.; Mongruel, A.; Royon, L.; Beysens, D. Grooves Accelerate Dew Shedding. *Phys. Rev. Lett.* **2019**, *122* (9), 098005. https://doi.org/10.1103/PhysRevLett.122.098005.
(53) Xie, D.; Sun, Y.; Wu, Y.; Wang, K.; Wang, G.; Zang, F.; Ding, G. Engineered Switchable-Wettability Surfaces for Multi-Path Directional Transportation of Droplets and Subaqueous Bubbles. *Adv. Mater.* **2023**, *35* (9), 2208645. https://doi.org/10.1002/adma.202208645.
(54) Bae, M.; Kang, Y.; Lee, D. W.; Jeon, D.; Ryu, J. Superaerophobic Polyethyleneimine Hydrogels for Improving Electrochemical Hydrogen Production by Promoting Bubble Detachment. *Adv. Energy Mater.* **2022**, *12* (29), 2201452. https://doi.org/10.1002/aenm.202201452.
(55) Xu, W.; Lu, Z.; Wan, P.; Kuang, Y.; Sun, X. High-Performance Water Electrolysis System with Double Nanostructured Superaerophobic Electrodes. *Small* **2016**, *12* (18), 2492–2498. https://doi.org/10.1002/smll.201600189.
(56) Trotochaud, L.; Ranney, J. K.; Williams, K. N.; Boettcher, S. W. Solution-Cast Metal Oxide Thin Film Electrocatalysts for Oxygen Evolution. *J. Am. Chem. Soc.* **2012**, *134* (41), 17253–17261. https://doi.org/10.1021/ja307507a.
(57) Bediako, D. K.; Lassalle-Kaiser, B.; Surendranath, Y.; Yano, J.; Yachandra, V. K.; Nocera, D. G. Structure–Activity Correlations in a Nickel–Borate Oxygen Evolution Catalyst. *J. Am. Chem. Soc.* **2012**, *134* (15), 6801–6809. https://doi.org/10.1021/ja301018q.
(58) Sivanantham, A.; Ganesan, P.; Shanmugam, S. Hierarchical NiCo2S4 Nanowire Arrays Supported on Ni Foam: An Efficient and Durable Bifunctional Electrocatalyst for Oxygen and Hydrogen Evolution Reactions. *Adv. Funct. Mater.* **2016**, *26* (26), 4661–4672. https://doi.org/10.1002/adfm.201600566.
(59) Wei, Y.; Shin, C.-H.; Tetteh, E. B.; Lee, B.-J.; Yu, J.-S. Insight into the Boosted Electrocatalytic Oxygen Evolution Performance of Highly Hydrophilic Nickel–Iron Hydroxide. *ACS Appl. Energy Mater.* **2020**, *3* (1), 822–830. https://doi.org/10.1021/acsaem.9b01952.

TOC Graphic